Multi-projection fusion system for special-shaped metal screen

Mingcong Ma[1], Yu Wang[1], Dongdong Guan[1,*], Chenglei Yang[1], Xiangxu Meng[1]
{201734818@mail.sdu.edu.cn, 16811170@qq.com,}
{ddguan@sdu.edu.cn, chl_yang@sdu.edu.cn, mxx@sdu.edu.cn}
[1]Shandong University, 1500 ShunHua Road, Jinan, 250101, China

Abstract. Curved metal projection screens are widely used in various places such as theme parks, museums, and art galleries due to their ability to produce highly immersive 3D stereoscopic projection effects. They have also become important interactive devices for constructing projection-based virtual reality systems. However, because metal screens have non-Lambertian reflection characteristics and the normal direction on the curved screen changes significantly, the brightness of the image seen by viewers at different positions varies remarkably. Traditional brightness fusion algorithms can only achieve brightness fusion from a single viewing angle, maintaining consistent brightness of the projected image under that single angle but fail to handle the significant changes in image brightness when viewers move during viewing. To address this issue, this paper proposes a multi-projection fusion system for large special-shaped metal screens. This system can not only effectively correct the geometric distortion of images on special-shaped metal screens but also perform real-time brightness fusion of the projected images according to the user's position. As a result, users can always see images with consistent brightness during mobile viewing, effectively enhancing the sense of reality and immersive experience.

Keywords: metal screen ; multi-projection system ; distortion correction ; brightness fusion

1 Introduction

Large-space projection environments are no longer limited to traditional flat diffuse reflection screens; the application of large-space special-shaped metal projection screens is growing rapidly. Metal screens not only enable high-quality polarized 3D display effects but also, through their large-space and special-shaped design, provide viewers with an enveloping, highly immersive VR viewing experience. As a result, they are widely used in 4D cinemas, theme parks, museums, and art galleries.

In such large-space projection-based VR display environments, viewers are no longer confined to the traditional viewing mode of sitting in fixed seats; instead, they can watch and interact while moving freely. References [1, 2, 3] propose a series of multi-user stereoscopic display technologies, which can provide independent 3D display effects for 2-6 users in the same projection area. This

IIKI 2025, December 18-21, Chengdu, People's Republic of China

DOI 10.4108/eai.18-12-2025.2365294

allows viewers to independently see 3D images that match their positions and perspectives while moving freely, thereby achieving a more realistic and immersive VR experience.

However, [1, 2, 3] focus mainly on technologies that provide independent 3D display effects for group users by modifying projector devices and 3D glasses, but do not address the issue of significant changes in the brightness of projected images when users move freely in the environment with special-shaped metal projection screens in large-space. Due to the non-Lambertian reflection characteristics of metal screens and the obvious changes in the normal direction on the curved screen, the brightness of the image seen by viewers at different positions varies significantly, which reduces the sense of reality and immersive experience.

Traditional multi-projection brightness fusion algorithms can only achieve brightness fusion from a single viewing angle, maintaining consistent brightness of the projected image under that single angle, but fail to handle the significant changes in image brightness when viewers move during viewing. As shown figures 1(a) and (b), even if the brightness of multiple projectors is correctly fused at the central position, when viewers watch from the left and right positions respectively, the image brightness on the curved metal screen still shows obvious inconsistency. Meanwhile, the Mach band phenomenon in the overlapping areas of the images from different projectors is also very prominent. To address this, this paper proposes a multi-projection fusion system for large special-shaped metal screens, which can perform brightness fusion of the projected images according to the user's position. This ensures that users can always see images with consistent brightness during mobile viewing, while also eliminating the Mach band phenomenon in the overlapping parts of the images from multiple projectors (as shown in figures 1(a) and (b)), thus effectively enhancing the sense of reality and immersive experience.

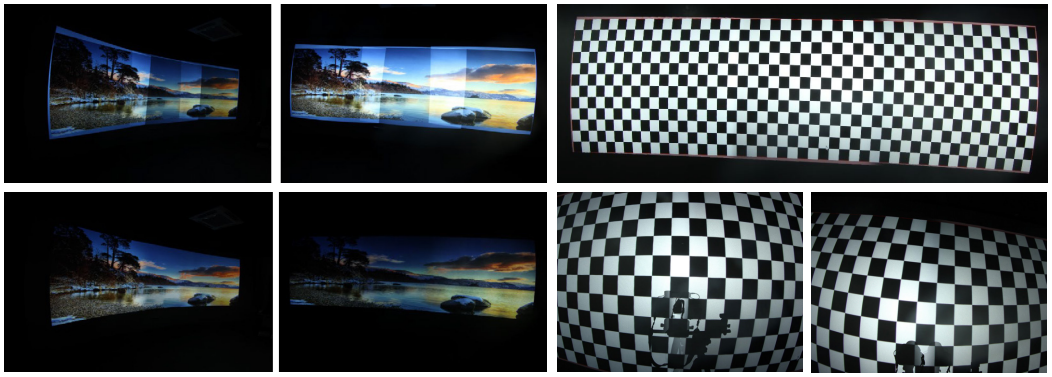

(a) (b) (c)

Fig. 1. Brightness fusion and geometric stitching of the multi-projection system. In (a) and (b), the upper (lower) images respectively show the effects before (after) brightness fusion as observed from the left and middle positions of the screen, and (c) The upper image shows the stitching result viewed from the middle position of the screen, while the two images below respectively display the stitching results of the non-overlapping area (left) and the overlapping area (right).

In addition, regarding the geometric distortion correction of curved projection screens, the method commonly used in current engineering is to realize image distortion correction by manually dragging and adjusting the positions of the corner points of the grid image. This manual correction method is extremely time-consuming and difficult to achieve precise correction when dealing with large-space special-shaped projection screen environments. Another method is to use a single camera to capture the image distortion and then perform automatic correction, but this method has the problem that the shooting angle of a single camera cannot cover the large-space special-shaped screen. To address this, this paper also proposes a method for image distortion correction based on 3D reconstruction of the special-shaped screen using a stereo fisheye camera pair (as shown in figures 1(c)), which improves the accuracy and efficiency of image distortion correction for large-space special-shaped projection screens. The main contributions of this paper are as follows:

- For the geometric correction and image stitching of multi-projection images on special-shaped screens, quadratic surface fitting is used to achieve continuous and complete 3D reconstruction, and implement arc length parameterisation for dimensionality reduction. On this basis, a one-to-one mapping relationship from the physical pixels of the projector to the pixels of the actual projected image is established.
- Regarding the brightness fusion problem, the concept of irradiance and human contrast perception are used to explain brightness, and corrections are performed for the RGB channels respectively to concentrate the image brightness in a relatively small brightness range as much as possible, thus realizing natural stitching of the projection area and a more comfortable and natural user experience.
- Based on the pre-measured brightness data of the special-shaped metal screen at several fixed positions, real-time multi-projection brightness fusion is achieved through position interpolation, ensuring that the brightness of the projected image seen by users remains consistent during free movement.

2 Related work

In multi-projection fusion systems, to ensure a favorable user experience and immersion, there are two primary issues that need to be addressed. On one hand, the problem of geometric stitching must be resolved to guarantee the integrity and seamlessness of the image. On the other hand, the aspect of brightness fusion requires attention, aiming to eliminate significant brightness differences so that users do not easily perceive that the projected image is formed by the combined projection of multiple projectors.

2.1 Geometric Correction

In general, within the research on geometric correction for multi-projection systems, the research trend has gradually shifted from traditional multi-projection geometric correction on flat screens [4, 5] to multi-projection geometric correction on curved special-shaped screens [6, 7].

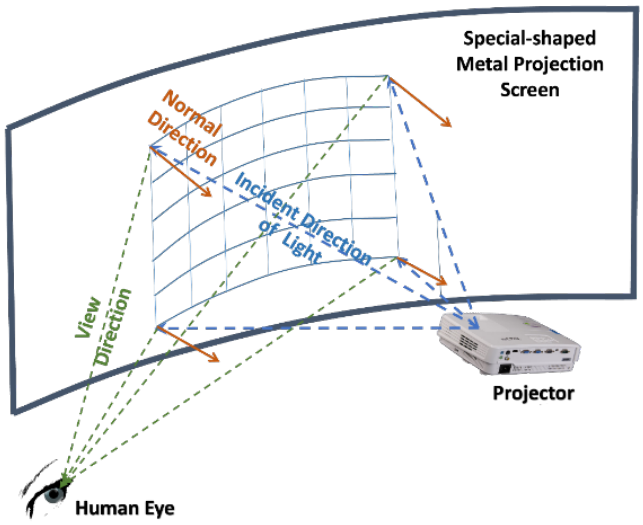

Fig. 2. Analysis of factors affecting image brightness on special-shaped metal projection screens.

Moreover, geometric correction methods have evolved from mechanical structure correction [8, 9] to camera-based geometric correction [10, 11]. The planar template algorithm proposed by Zhang et al. [12, 13] is a currently widely used camera calibration algorithm; it is also a relatively mature algorithm and serves as the foundation for most parametric geometric correction methods.

Currently, camera-based geometric correction is a highly accurate method. In this approach, camera calibration is first required to determine the intrinsic and extrinsic parameters of a single camera or camera arrays. Subsequently, the calibrated cameras are used to capture feature images on the screen to obtain the geometric description of the screen. Feature images on the screen exist in various forms; earlier methods generally tended to set up physical feature images on the screen through various means[14, 15], whereas contemporary approaches favor projecting feature images onto the screen[16, 17]. Among these, within the method of projected feature images, projected structured light images are a key focus of research. Numerous studies have employed various structured light methods to achieve geometric stitching and calibration of multi-projection systems[18, 19].

Specifically in this context, Raskar et al.[20] proposed a method that uses a single camera to achieve geometric correction and image stitching of multiple projectors by calculating the correspondences among the projection space, camera space, and display space. However, this method is only applicable to flat screens. Starkweather et al.[21] proposed a novel hardware environment scheme, which implements its own geometric stitching and fusion functionalities. Nevertheless, this scheme lacks good versatility and is difficult to apply in other existing hardware environments. The works of

Raskar et al.[22] and Baar et al.[23] share similarities: both achieve fusion of multi-projection systems via cameras and, to some extent, break free from the constraints of physical space. However, these methods require combining projectors and cameras to form a projection-capturing hardware setup, which results in high construction difficulty and substantial modification costs for existing hardware environments. Sajadi et al.[24] treat projectors as inverse cameras of the pinhole model, thereby realizing calibration and parameterization of projectors. Nevertheless, this method itself requires ensuring that the screen is a vertical cylinder and that the aspect ratio of the rectangle formed by the four corners of the screen is known. These preconditions have, to some extent, limited the versatility of the method. Similarly, Xizuo et al.[25] also treat projectors as inverse cameras of the pinhole model and achieve geometric reconstruction of the screen by projecting Gray codes. However, traditional Gray codes, due to their inherent limitations, perform poorly on screens with high gain factors. Askarian et al.[26] and Shuaihe Zhao et al.[27] also use Gray codes to realize screen reconstruction, but they are similarly not well-suited for screens with a high-gain coefficient. Zhao, S et al.[28] proposed a novel structured light method, which can avoid the drawbacks of traditional structured light methods to a certain extent and thus achieve normal operation even under high-gain screen conditions. Nevertheless, structured light methods themselves are limited by the accuracy of capture, often resulting in errors during pixel-level capture and processing, which makes it impossible to achieve dense reconstruction of projected points on the screen. Wang X et al.[29] employed the Bessel surface model to fit continuous curved screens for reconstructing the geometric structure of the screen. However, this method also suffers from the issue of sparse reconstruction, as it only reconstructs partial position information on the screen.

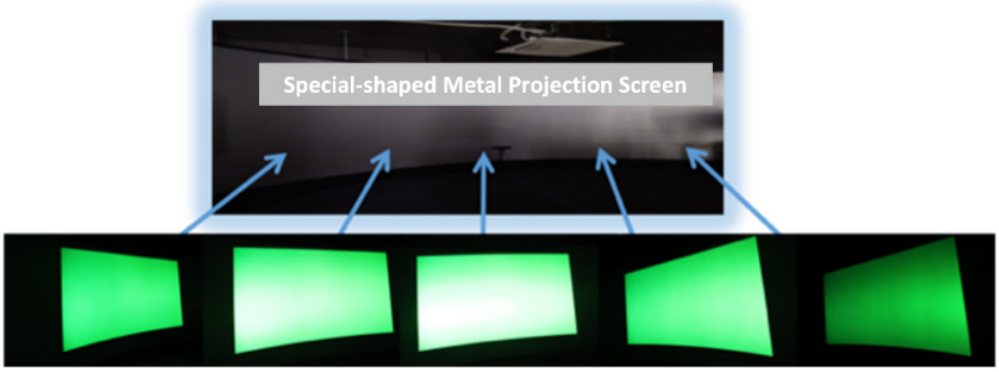

Fig. 3. Variations in image brightness on special-shaped metal projection screens.

2.2 Brightness Fusion

In terms of brightness fusion, Huang et al.[30] offset the influence of non-white projection surfaces on the color of projected images through visual cognitive radiometric compensation, while

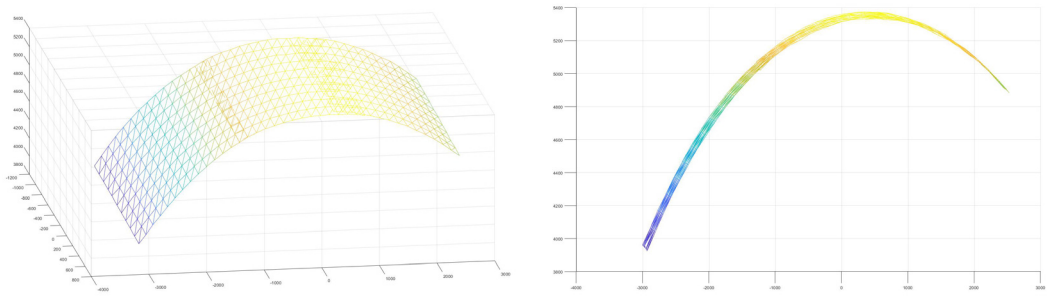

Fig. 4. The sparse 3D feature points.

restoring the color details of input images on flat projection planes with different base colors as much as possible. Heinz et al.[31] proposed an efficient algorithm for measuring the color transfer function of display devices or projection devices. Compared with previous related algorithms, it improves the speed by one to two orders of magnitude without losing precision. Christoffer et al.[32] proposed a realistic color reconstruction algorithm that considers physical factors such as ambient light, projection surface material, projector position, and projector color model in the context of spatial augmented reality applications. It adjusts projection parameters based on a pixel-based 3D lookup table to achieve realistic color reproduction. The Projectibles method proposed by Brett et al.[33] algorithmically segments videos into static printed images and dynamic projected video images. The combination of these two components significantly enhances the color contrast of images and, to a certain extent, improves the resolution of videos. Pjanic et al.[34] leverage the property that the human eye perceives dense discrete points of the same color as continuous color. By combining high-frequency printed images with projected images, they achieve reasonable variation and dynamic adjustment of projected colors, and can also realize some special visual effects.

Aditi et al.[35] proposed a per-pixel radiometric correction method, which performs equalization processing on brightness differences between projectors and within individual projectors in multi-projection systems, aiming to enhance users' full immersive experience in multi-projection systems. Mahesh et al.[36] proposed a method using threshold maps to predict the maximum tolerable brightness error at each position on the image. In their research model, three main characteristics of the visual system are employed: threshold sensitivity, contrast sensitivity, and contrast masking, with image synthesis performed based on reducing perceived errors. Wang et al.[37], aiming to enhance the quality of projected display images and reduce unnaturalness, combined threshold maps with the three characteristics of the human visual system and proposed an optimization method that compresses input contrast while maintaining the compression ratio. Aditi et al.[38] studied the mathematical model of human contrast perception and, considering the spatial variations in projection displays, proposed an optimized projection method targeting seamless display. Building on previous work, this method smoothly expanded the dynamic range of displayed images as much as possible by adjusting the maximum allowable brightness value of each pixel, under the premise that humans cannot perceive obvious differences. However, this work sets the fitting function for all

pixels with the same parameters, differing only in the scaling range. Debevec et al.[39] proposed a method to reconstruct irradiance from multiple photos with different exposure levels and subsequently construct high dynamic range scenes. This method serves as the foundation for subsequent irradiance-related approaches.

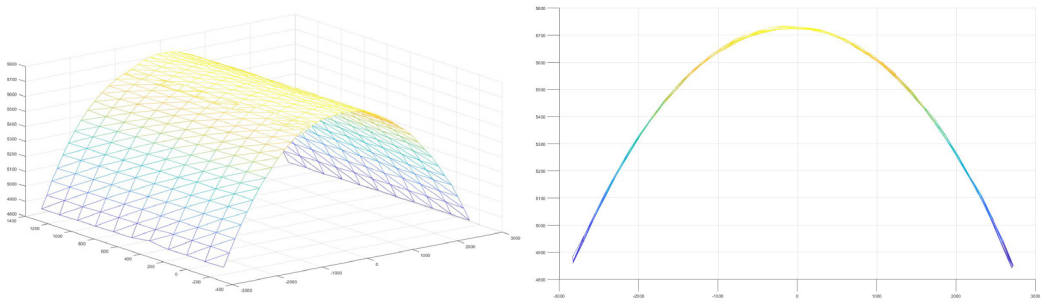

(a) (b)

Fig. 5. The sparse 3D feature points after PCA. (a) Front view of the sparse 3D feature point set after PCA. (b) Top view of the sparse 3D feature point set after PCA.

3 Analysis of Light Reflection Characteristics of Special-Shaped Metal Projection Screens

In a projection display environment, the intensity of image brightness mainly depends on four factors: the material properties of the screen, the incident direction of the light source, the normal direction of the screen, and the view direction. This section analyzes the light reflection characteristics of special-shaped metal projection screens.

First, metal projection screens are made by coating a substrate with metal particle coatings, which exhibit significant non-Lambertian reflection characteristics. Thus, they can maintain the polarization characteristics of incident light, which is a necessary condition for the realization of stereoscopic projection. In industrial production, the light reflection characteristics of metal screens are generally measured by the gain index of the screen. The so-called screen gain refers to the ratio of the reflected light intensity at the center of the metal screen to that of a completely diffuse reflective screen when the light source is incident vertically. To achieve polarized stereoscopic projection, the gain coefficient of the metal screen must be at least 2.0. The cost of high gain is that the reflected light intensity of the metal screen varies significantly at different viewing positions. For a flat metal screen with a gain coefficient of 2.0, when the light is incident vertically, the brightness of the reflected light seen by the viewer will decrease by about 50% when the angle between the viewer's view direction and the screen normal exceeds 30 degrees.

Next, we examine the influence of the incident direction of the light source and the normal direction of the screen. A projector is not a parallel light source; the projection light is emitted from the center of the projector in a cone shape toward the screen, so the incident light direction at each

point on the screen is different. Meanwhile, the normal direction at each point on the special-shaped screen is also different. Therefore, even when the projector displays a monochromatic image with uniform brightness, the brightness of the image on the screen is uneven.

Finally, there is the influence of the view direction. When viewers move freely in the projection environment with large-space special-shaped metal screens, the brightness of the projected image will change as the viewing position changes. The influence of the above four factors on the brightness of the projected image is shown in figures 2.

Figures 3 shows the image brightness observed at different positions when a single projector displays a uniformly bright pure green image on an annular metal projection screen. At the same viewing position, the image brightness is uneven due to the properties of the metal screen material, changes in the incident light direction, and variations in the screen normal. Moreover, as the viewing position changes, the image brightness also undergoes significant changes.

Furthermore, in a large-space projection environment, the projection area of a single projector cannot cover the entire screen area, so multiple projectors are required for spliced projection display. In this case, the image brightness in the overlapping projection area of two projectors will be significantly higher than that in the non-overlapping area. At this point, it is necessary to reasonably reduce the image brightness in the overlapping projection area to eliminate the Mach band effect and maintain consistent image brightness on the screen.

Traditional multi-projection brightness fusion algorithms can only achieve brightness fusion from a single viewing angle, maintaining consistent brightness of the projected image and eliminating the Mach band effect under that single angle. For example, in IMAX theaters and 4D cinemas, multi-projection brightness fusion is only performed at the central position of the seating area. However, when viewers move to watch and interact, even if the brightness is correctly fused at the central position, the image brightness will still change significantly as the viewing position shifts, and the Mach band effect cannot be eliminated, as shown in figures 1. To address this issue, the multi-projection brightness fusion algorithm proposed in this paper can perform multi-projection brightness fusion according to different viewing positions of the audience, maintaining consistent brightness of the projected image, thereby enhancing the sense of reality and immersive experience.

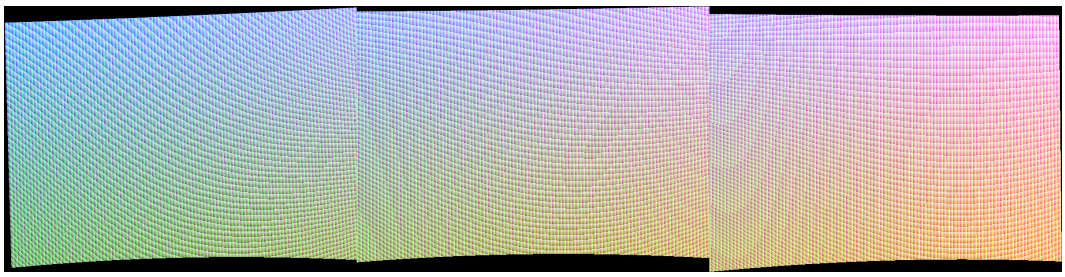

Fig. 6. Encoded image of arc length parameterization.

4 Multi-Projection Fusion Algorithm

This section describes the multi-projection brightness fusion algorithm proposed in this paper for the environment with special-shaped metal projection screens. Section 4.1 presents the image geometric distortion correction algorithm, Section 4.2 introduces the image brightness fusion algorithm at specified measurement positions, and Section 4.3 describes the method for realizing multi-projection brightness fusion during viewers' moving viewing through position interpolation calculation.

Through the algorithm in Section 4.1, the one-to-one correspondence between projector pixels and image pixels can be obtained in the projector coordinate system, and arc length parameterization processing is performed, thereby completing the distortion correction of the projected image. Meanwhile, this serves as the basis for the algorithms in Sections 4.2 and 4.3. In Section 4.2, according to the one-to-one correspondence between projector pixels and image pixels, the spatial position of the specified measurement position in the projector coordinate system is obtained, and the brightness fusion parameters at each measurement position are calculated. In Section 4.3, based on the one-to-one correspondence between projector pixels and image pixels, the conversion relationship between the depth camera coordinate system (used for tracking the viewer's position) and the projector coordinate system is obtained through shooting and measurement. Real-time multi-projection brightness fusion is realized through position interpolation calculation.

Fig. 7. Pure grayscale images with uniformly increasing brightness.

4.1 Distortion Correction

Projected images suffer significant geometric distortion on special-shaped screens. The distortion correction algorithm proposed in this paper first performs 3D reconstruction of the special-shaped screen using a stereo fisheye camera, followed by projector calibration and quadratic surface fitting of the special-shaped screen. This process establishes a one-to-one correspondence between projector pixels and image pixels, and further realizes arc length parameterization of projector pixels in the projector coordinate system, thereby achieving geometric correction of the projected image.

First, the projector displays a standard checkerboard pattern on the special-shaped metal screen. The calibrated stereo fisheye camera performs 3D reconstruction on the checkerboard corners of the special-shaped screen, obtaining a set of sparse 3D feature points on the screen surface. Based on this set of feature points, the projector can be calibrated using the pinhole camera model, and the Taubin method is used for quadratic surface fitting of the special-shaped screen. Then, according to the projector calibration results, spatial intersection calculation is performed between the projection ray of each projector pixel and the parameter equation of the screen surface to establish a one-to-one correspondence between projector pixels and image pixels, and obtain the arc length parameterization results of the projector pixels. On the playback server, the input image is sampled according to the arc length parameterization results of the projector pixels and then played back, realizing the distortion correction of the projected image.

The calibration of the stereo fisheye camera adopts the classic method given in [9], and the calibration data collection and the collection of projection feature points on the screen surface are completed by capturing checkerboard images. Due to considerations of calibration accuracy and shooting field of view, stereo fisheye cameras are selected as the shooting equipment, and the calibration procedure uses Matlab's camera calibration toolbox. Then, the calibrated stereo fisheye camera performs 3D reconstruction on the checkerboard corners of the special-shaped screen, obtaining a set of sparse 3D feature points on the screen surface, as shown in figures 4.

As can be seen from figures 4(b), although the screen is roughly perpendicular to the ground in physical space, in the coordinate system formed by camera calibration, there is a certain offset from the world coordinate system due to the uncontrollable orientation of the camera. Therefore, principal component analysis (PCA) processing is required to adjust the coordinate axes so that they are consistent with the world coordinate system. The recovered diagram of the screen surface coefficients after PCA processing is shown in figures 5.

As can be seen from figures 5(b), the sparse 3D feature point set is roughly perpendicular to the ground, making it possible to separate the y-coordinate from the x and z coordinates. By fitting the processed point set using the Taubin method, the surface equation of the screen can be obtained, which is in the form shown in (1), where the y-coordinate is independent of the x and z coordinates.

$$x = \phi(t), y = y, z = \psi(t) \tag{1}$$

Based on the 3D sparse feature point set, the projector can be calibrated using the methods described in [12, 13] to obtain its intrinsic and extrinsic parameters. Then, based on these parameters, the intersection of the projection ray of each projector pixel with the screen surface equation is calculated, and the x, y, z coordinates of the intersection point in the projector coordinate system are

determined, thereby establishing a one-to-one correspondence between projector pixels and image pixels. The above process is performed for each projector in the projection environment, and one projector is selected as the main projector. The extrinsic parameters of other projectors are uniformly transformed to the coordinate system of the main projector through coordinate system conversion.

Subsequently, arc length parameterization is performed on the projector pixels. The arc length s is calculated using the x and z coordinates of the intersection point between the projection ray and the screen surface, which serves as the u parameter of the projector pixel, as shown in (2) and (3):

$$ds = \sqrt{(dx)^2 + (dz)^2} = \sqrt{\phi'^2(t) + \psi'^2(t)} \tag{2}$$

$$s = \int_{\alpha}^{\beta} \sqrt{\phi'^2(t) + \psi'^2(t)} dt \tag{3}$$

The y-coordinate of the intersection point is taken as the v parameter of the projector pixel, resulting in the arc length parameterization, as shown in (4):

$$u = s, v = y \tag{4}$$

After obtaining the arc length parameterization of projector pixels, the overlapping projection areas between projectors can also be determined. On the playback server side, according to the arc length parameterization results of projector pixels, the input image is resampled and displayed by the GPU, thus completing the distortion correction of the projected image. During actual operation, the arc length parameterization data is encoded into a color image and input to the GPU. The R and G values of each pixel are used to encode the u-coordinate of that pixel, and the B and A values are used to encode the v-coordinate. The specific encoding method is shown in (4), and the generated encoded image is presented in figures 6.

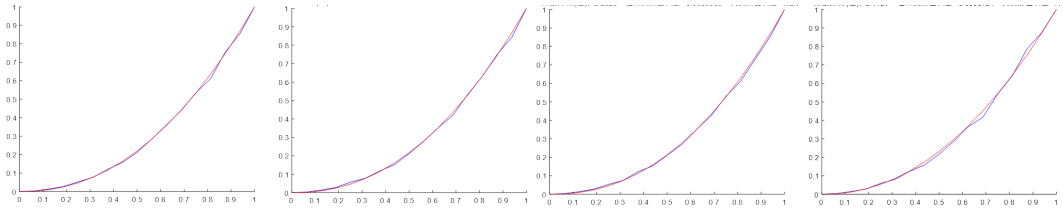

Fig. 8. Discrete correspondence curves between normalized input brightness and actual irradiance.

4.2 Multi-Projection Brightness Fusion at Specified Positions

As analyzed in Section 3, the image brightness on the special-shaped metal projection screen not only changes with the viewing position but also shows inconsistency even when viewed from a fixed position. To address this, this paper adopts the following brightness fusion method: the projectors display a set of pure grayscale images with uniformly increasing brightness, and then several

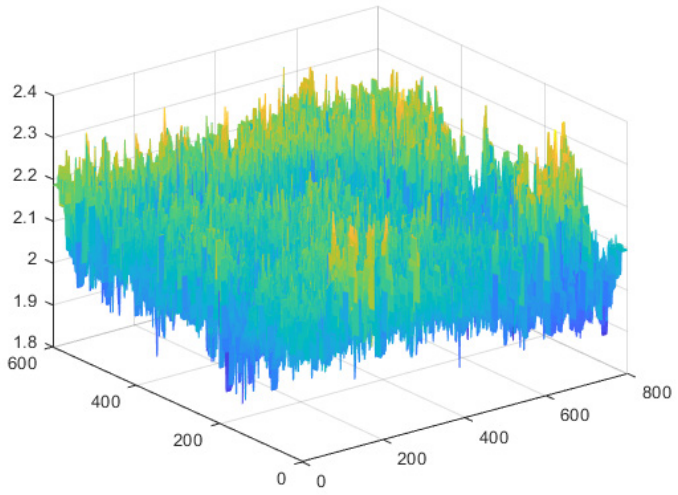

Fig. 9. Fitting results of exponent t.

measurement positions are selected. At each measurement position, a camera is used to capture this set of pure grayscale images, so as to obtain the discrete correspondence between the input brightness values of projector pixels and the actual irradiance on the screen. Curve fitting is then performed to calculate the brightness correction coefficients at each measurement position, thereby completing brightness fusion at each measurement position. In Section 4.3, the depth camera is used to track the viewer's position in real time, and position interpolation calculation is performed based on the brightness correction coefficients at each measurement position to obtain the corresponding brightness correction coefficients, realizing multi-projection brightness fusion during the viewer's moving viewing process.

At each measurement position, the projector first displays a standard checkerboard pattern, which is captured by a camera with calibrated internal parameters. Since the x, y, z coordinates of the checkerboard corners in the projector coordinate system have been calculated and saved in Section 4.1, these checkerboard corners can be used to calibrate the external parameters of the camera, obtaining the spatial position of the camera in the projector coordinate system. In Section 4.1, a one-to-one correspondence between projector pixels and image pixels on the screen has been established; therefore, a one-to-one correspondence between projector pixels and pixels in the camera-captured images can be established through the projection of image pixels on the screen onto the camera's imaging plane.

Subsequently, the projector sequentially displays 17 pure grayscale images with grayscale values uniformly increasing from 0 to 255, as shown in figures 7, which are then captured by the camera. Using the method in [36], based on the camera response function (CRF) and the corre-

spondence between projector pixels and pixels in the camera-captured images (calculated separately for the RGB channels), the discrete correspondence curves between the input brightness of each projector pixel and the actual irradiance are obtained. Each discrete correspondence curve consists of 17 sampling points, corresponding to the 17 levels of pure grayscale image inputs in figures 7. On the special-shaped metal screen, due to changes in the incident light direction and the normal direction of the screen, the discrete correspondence curve of each pixel is different. However, after normalizing both the input brightness and irradiance to the range [0, 1], they all show an obvious power function shape. figures 8 shows the discrete correspondence curves between input brightness and actual irradiance in the R channel for 4 randomly selected projector pixels.

The discrete correspondence curves are fitted using the power function:

$$R = W_{ij} g^t \tag{5}$$

where R is the irradiance obtained from shooting measurements, W_{ij} represents the maximum achievable irradiance of the pixel (i.e., the irradiance corresponding to the maximum input brightness), g is the input brightness of the pixel, and the exponent t is the coefficient to be fitted. The exponent t can be fitted using the 17 sampling points on the discrete correspondence curve. Each projector pixel corresponds to a different exponent t, with values roughly ranging from 1.8 to 2.4, as shown in figures 9.

The goal of brightness fusion is to make the irradiance of each pixel roughly the same in the user's eyes. Therefore, for each pixel, the relationship between the irradiance before and after brightness fusion is as follows:

$$R' = \frac{W_m}{W_{ij}} R \tag{6}$$

where R is the irradiance of the pixel before brightness fusion, R' is the irradiance of the pixel after brightness fusion, and W_m represents the maximum allowable irradiance of the pixel, which is solved using the smoothing method based on the human contrast perception limit given in [35]. For each pixel, if the W_m values of its neighboring pixels can be maintained within a small range, it can ensure that the brightness observed by the user remains basically consistent. Combining (5) and (6), we can get:

$$R' = W_m g^t \tag{7}$$

Equation (7) gives the relationship between the input brightness value g and the irradiance R' after brightness fusion. Since the fused irradiance R' and its corresponding input brightness value g' also satisfy a power function relationship, that is:

$$R' = W_{ij} g'^t \tag{8}$$

Combining (7) and (8), we can obtain:

$$g' = \lambda g, \lambda = \sqrt[t]{\frac{W_m}{W_{ij}}} \tag{9}$$

Here, λ is the brightness correction coefficient of the pixel at this position. Both the power exponent t and the maximum allowable irradiance W_{ij} are constants, and W_m can also be obtained through pre-calculation.

The calculation of brightness coefficients in the overlapping area of projector images is relatively complex and needs to be realized by adjusting W_m in (9). The following will discuss how to adjust W_m in the overlapping area. Since irradiance satisfies additivity, that is, if a point on the screen receives light from multiple projectors, its irradiance is equal to the sum of the irradiances of each projector's light source at that point. Therefore, for a point in the overlapping area, its allowable total irradiance W_m needs to be allocated to the multiple projectors projecting on that point, and the allocation rules are shown in figures 10.

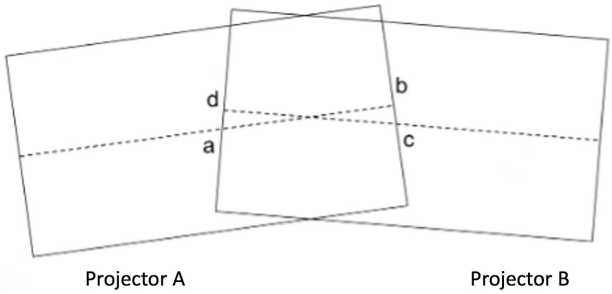

Fig. 10. Irradiance allocation in the overlapping area of projectors.

figures 10, the solid rectangles represent the projection areas of Projector A and Projector B, respectively, the hexagonal area in the middle is the overlapping area, and the two dashed lines represent a row of pixels in Projector A and Projector B, respectively. For the row of pixels represented by the dashed line in Projector A, point a is the starting pixel of the overlapping area, and point b is the ending pixel of the overlapping area. From point a to point b, the corresponding W_m value will linearly decrease to zero. Similarly, for Projector B, from point c to point d, the corresponding W_m value will linearly decrease to zero. Such a dynamic allocation scheme essentially weakens the influence of projectors on the edges, making only a single projector actually function at the edges of the overlapping area, thus eliminating the light and dark changes at the boundary of the overlapping area.

Since the correction coefficient λ is a floating-point number in the interval [0, 1], it can be saved as an image without encoding, as shown in figures 11.

4.3 Multi-Projection Brightness Fusion for Viewers on the Move

In Section 4.2, the multi-projection brightness correction coefficients at specified measurement positions are obtained. On this basis, the depth camera is used to track the viewer's position in real time, and position interpolation calculation is performed according to the brightness correction coefficients at each measurement position to obtain the corresponding brightness correction coefficients,

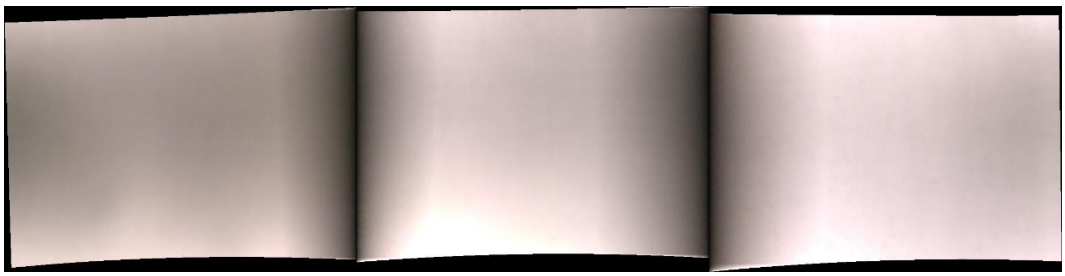

Fig. 11. Result diagram of brightness correction coefficients.

thereby realizing multi-projection brightness fusion during the viewer's mobile viewing process.

To this end, it is first necessary to convert the coordinate system of the depth camera to the projector coordinate system, which can be achieved using the method in Section 4.2 for calculating the position of the camera in the projector coordinate system. 6-9 sampling positions are selected, and the camera is used to capture the standard checkerboard pattern displayed by the projector to determine the spatial position of the camera in the projector coordinate system. Then, the spatial position of the camera in the depth camera coordinate system is manually marked, based on which the coordinate system of the depth camera is converted to the projector coordinate system.

During the user's movement, the depth camera device is used to capture the user's current position in real time. Interpolation operations are performed based on the user's current position and the measurement positions in Section 4.2 to calculate the correction coefficient for each projector pixel at the user's current position in real time. The original input pixels can then be processed using the correction coefficient matrix in the manner specified by (9). The above calculation process is also carried out in the Shader, utilizing GPU acceleration to ensure the real-time performance of brightness fusion.

5 Experimental Results

Based on the above scheme, we designed relevant experiments to verify the performance and behavior of the system, enabling users to observe an integrated image with consistent brightness while moving freely in front of the special-shaped metal screen.

Since the camera is not allowed to adjust parameters other than the exposure time after calibration, and shaking should be avoided as much as possible during the shooting process, a remote control shutter is used for actual shooting to reduce unnecessary contact. During the shooting of grayscale gradient images, it is necessary to ensure that no overexposure occurs in each image. Therefore, different exposure times need to be used for shooting images of different grayscales at different positions, and the specific exposure time needs to be adjusted according to the camera performance and screen characteristics. A set of exposure time examples used in the system is given below, as shown in Table 1.

The projection screen is an arc-shaped metal screen, and the projector model is BenQ W2000

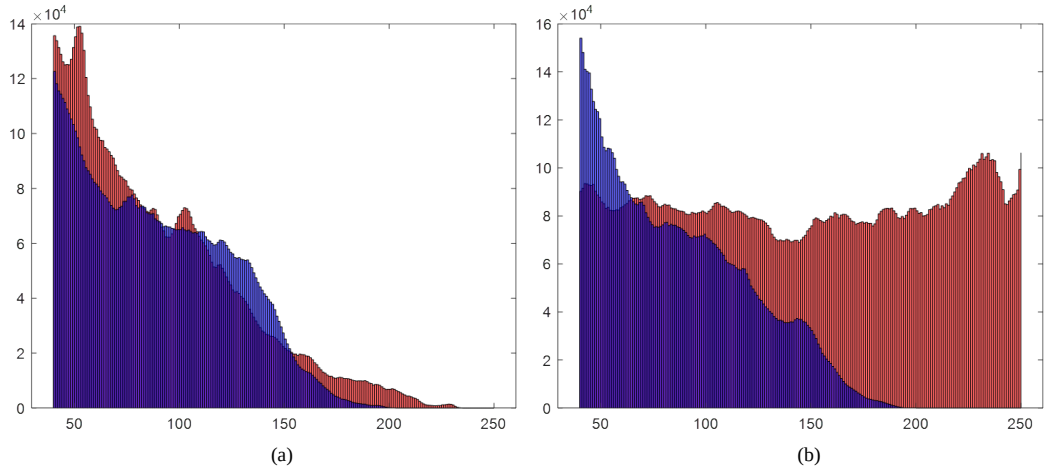

Fig. 12. Results of histogram analysis before and after brightness fusion. (a) Hitogram of left View, (b) histogram of middle view.

Table 1. Grayscale-Exposure Time Correspondence Table

Grayscale	0	16	32	48	64	80	96	112	128	144	160	176	192	208	224	240	255
Exposure	30	30	30	6	6	2.5	2.5	1.3	1.3	0.8	0.8	0.5	0.5	0.4	0.4	0.25	0.25

with a physical resolution of 800*600. The depth camera device used is Microsoft Kinect 2.0. For the shooting work, a Canon 550D digital camera was selected, with a shooting image resolution of 3456x5184. The lens used is the Canon EF 8-15mm F4 L Fisheye USM fisheye lens along with the matching Canon EW77 lens hood. The software environments used in the experiment are Matlab R2018b and Unity3D 2018.3.0f2.

First, the system was tested from the user's visual perspective. The test results are shown in figures 1, where figures 1(a) and figures 1(b) are the brightness fusion results at different positions, respectively, figures 1(c) is the result of multi-projection geometric stitching.

Second, we use brightness histograms to evaluate the results of brightness fusion from objective data. Since there are black areas outside the projection range, the histogram analysis only intercepts the distribution interval of valid pixels, as shown in figures 12.

Figures 12(a) shows the results of separate histogram analyses of the two images before and after brightness fusion in figures 1(a), where the red histogram represents the image before brightness fusion in figures 1(a), and the blue histogram represents the image after brightness fusion in figures 1(a). Figures 12(b) shows the results of separate histogram analyses of the two images before and after brightness fusion in figures 1(b), where the red histogram represents the image before brightness fusion in figures 1(b), and the blue histogram represents the image after brightness fusion

in figures 1(b).

Figures 12(a), the maximum brightness of the blue histogram is around 200 with a relatively small number of pixels; the maximum brightness of the red histogram is around 230 with a relatively larger number of pixels. The result of this histogram analysis is not obvious, which is caused by the low overall brightness of both images. Although there is a significant difference in brightness between the two from the user's subjective perspective, this difference is not obvious in the histogram analysis. In figures 12(b), the red histogram is evenly distributed over the global interval without obvious aggregation or numerical peaks; the blue histogram is concentrated in a smaller brightness interval. This histogram result manifests as an obvious brightness difference before and after brightness fusion in visual perception.

After figures 12 analyzes the histogram differences before and after brightness fusion at the same position, the next step is to analyze the histogram results of different positions after brightness fusion, as shown in figures 13.

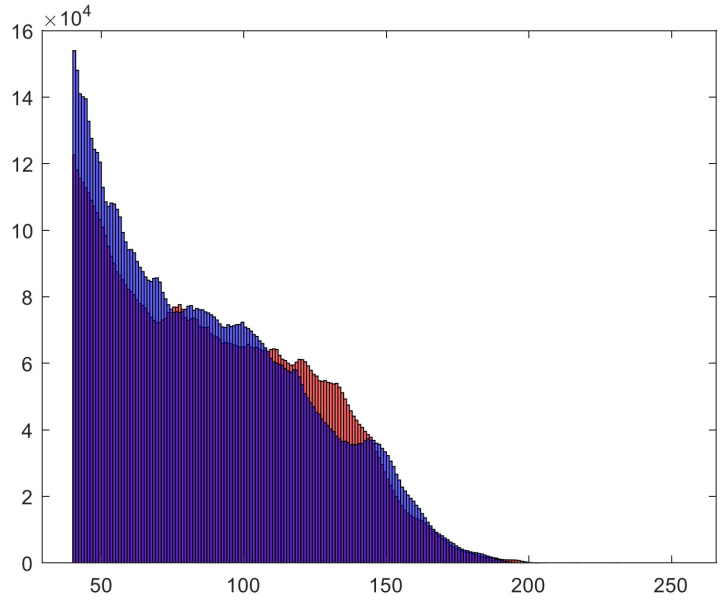

Fig. 13. Histogram analysis results of different positions after brightness fusion.

In figures 13, the red histogram corresponds to the result of the image after brightness fusion in figures 1(a), and the blue histogram corresponds to the result of the image after brightness fusion in figures 1(b). Similar to figures 12, due to the presence of black areas outside the projection range, the histogram analysis only intercepts the distribution interval of valid pixels. It can be seen from figures 13 that the blue histogram has a slightly higher distribution in the lower pixel interval, while the red histogram has a slightly higher distribution in the higher pixel interval, but the overall pixel distribution remains consistent. This histogram result manifests as a roughly identical bright-

ness experience in visual perception, which indicates that the images observed at different positions maintain brightness consistency.

We also discussed the real-time performance of the algorithm. Since the brightness correction coefficients for each camera position have been pre-calculated, only interpolation based on the position captured by Kinect is required during the runtime phase, resulting in relatively low real-time computing pressure. Under the aforementioned hardware and software environment, Unity can stably output 60 frames per second. In the future work, we can continue to explore more effective algorithms.

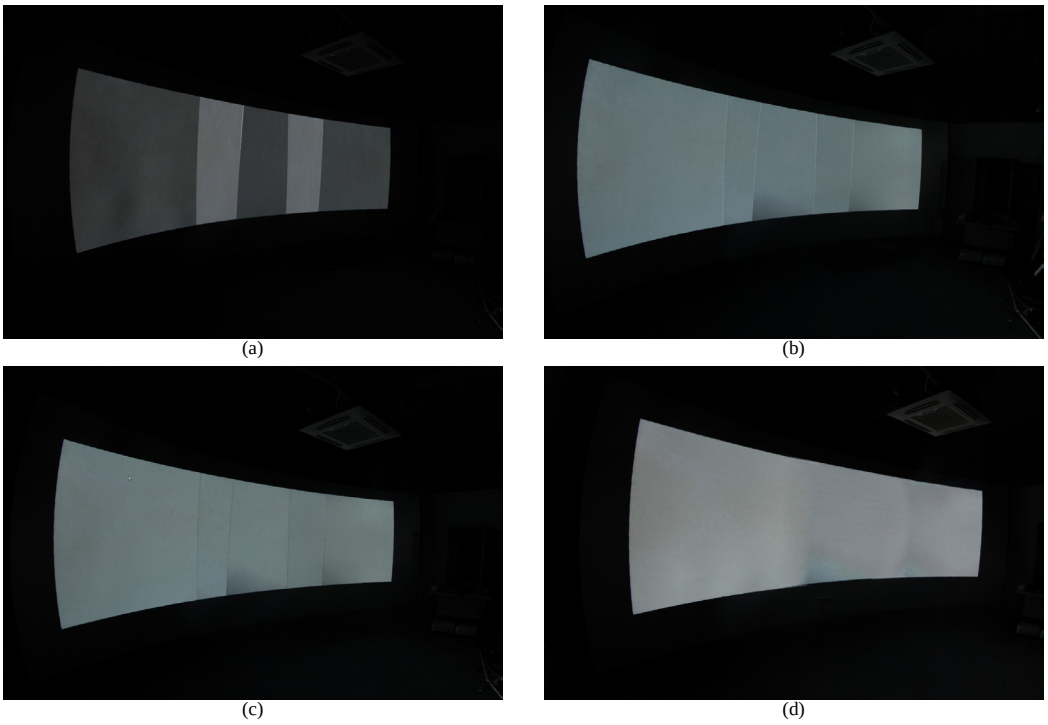

Fig. 14. Ablation experiment of brightness fusion.

In the ablation experiments, we compared the visual differences between various brightness fusion schemes, with the results shown in figures 14. Figures 14(a) shows the visual result without brightness fusion, where the overlapping areas exhibit noticeable abnormal brightness. Figures 14(b) shows the static pixel scheme, which adjusts the brightness of each pixel in the overlapping areas based on geometric correction results. This scheme produces a distinct bright line along the edges of the overlapping areas. To mitigate the bright line issue in figures 14(b), we apply one pixel indentation in pixel selection for the overlapping areas, thereby excluding the outermost pixels, shown in figures 14(c). This result exhibits a pronounced dark line along the edges of the overlapping

area. Finally, the result of our distance-based dynamic brightness fusion method is presented in shown in figures 14(d). The overlapping areas are no longer obvious, the edges are not clearly demarcated, and the visual continuity is better.

6 Conclusion and Discussion

The multi-projection fusion system for special-shaped metal screens proposed in this paper performs geometric correction, image stitching, and brightness fusion for multi-projection systems on special-shaped screens without changing the existing hardware conditions. It has achieved good results in image stitching and brightness fusion, enhanced users' sense of immersion and comfort, and features a relatively streamlined overall process, endowing the system with good maintainability and repeatability.

However, the current calibration process and shooting methods of the system need further optimization. Specifically, most of the workload in the current system implementation is concentrated in the shooting phase; therefore, formulating a more efficient and reasonable shooting workflow will help further reduce the system's time and labor costs. At present, the system needs to restart all processes from scratch when reconducting fusion work and cannot utilize existing stitching or fusion results for assistance. Thus, consideration can be given to adding specific calibration procedures to recalibrate the overall system at a lower cost after fusion is achieved. The dynamic irradiance allocation scheme in the brightness fusion part currently uses the distance to the edges on both sides as the benchmark, but there is still room for discussion regarding the benchmark and method of irradiance allocation. For example, the minimum distance to the edge of the overlapping area could be used as the benchmark, or a cosine function could be adopted for irradiance allocation instead of linear allocation. In summary, the system still has room for further optimization and improvement, and supplementary enhancements will be considered in the future.

Acknowledgments

Corresponding author: Dongdong Guan.

Declaration on Generative AI

The author(s) have not employed any Generative AI tools.

References

[1] Yu HD, Li HY, Sun WS, Gai W, Cui TT, Wang CT, et al. A two-view VR shooting theater system. In: Proceedings of the 13th ACM SIGGRAPH International Conference on Virtual-Reality Continuum and its Applications in Industry. Shenzhen China: ACM; 2014. p. 223-6. Available from: https://dl.acm.org/doi/10.1145/2670473.2670497.

[2] Kulik A, Kunert A, Beck S, Reichel R, Blach R, Zink A, et al. C1x6: a stereoscopic six-user display for co-located collaboration in shared virtual environments. In: Proceedings of the 2011 SIGGRAPH Asia Conference. Hong Kong China: ACM; 2011. p. 1-12. Available from: https://dl.acm.org/doi/10.1145/2024156.2024222.

[3] Guan D, Yang C, Sun W, Wei Y, Gai W, Bian Y, et al. Two Kinds of Novel Multi-user Immersive Display Systems. In: Proceedings of the 2018 CHI Conference on Human Factors in Computing Systems. Montreal QC Canada: ACM; 2018. p. 1-9. Available from: https://dl.acm.org/doi/10.1145/3173574.3174173.

[4] Allard J, Gouranton V, Lecointre L, Limet S, Melin E, Raffin B, et al. FlowVR: A Middleware for Large Scale Virtual Reality Applications. In: Hutchison D, Kanade T, Kittler J, Kleinberg JM, Mattern F, Mitchell JC, et al., editors. Euro-Par 2004 Parallel Processing. vol. 3149. Berlin, Heidelberg: Springer Berlin Heidelberg; 2004. p. 497-505. Series Title: Lecture Notes in Computer Science. Available from: http://link.springer.com/10.1007/978-3-540-27866-5_65.

[5] Raffin B, Soares L, Tao Ni, Ball R, Schmidt GS, Livingston MA, et al. PC Clusters for Virtual Reality. In: IEEE Virtual Reality Conference (VR 2006). Alexandria, VA, USA: IEEE; 2006. p. 215-22. Available from: http://ieeexplore.ieee.org/document/1667647/.

[6] Mine MR, Van Baar J, Grundhofer A, Rose D, Yang B. Projection-Based Augmented Reality in Disney Theme Parks. Computer. 2012 Jul;45(7):32-40. Available from: http://ieeexplore.ieee.org/document/6193074/.

[7] Sun W, Sobel I, Culbertson B, Gelb D, Robinson I. Calibrating multi-projector cylindrically curved displays for "wallpaper" projection. In: Proceedings of the 5th ACM/IEEE International Workshop on Projector camera systems. Marina del Rey California: ACM; 2008. p. 1-8. Available from: https://dl.acm.org/doi/10.1145/1394622.1394624.

[8] Allen W, Ulichney R. 47.4: Invited Paper: Wobulation: Doubling the Addressed Resolution of Projection Displays. SID Symposium Digest of Technical Papers. 2005;36(1):1514. Available from: http://doi.wiley.com/10.1889/1.2036298.

[9] Damera-Venkata N, Chang NL. Realizing Super-Resolution with Superimposed Projection. In: 2007 IEEE Conference on Computer Vision and Pattern Recognition. Minneapolis, MN, USA: IEEE; 2007. p. 1-8. Available from: http://ieeexplore.ieee.org/document/4270461/.

[10] Raskar R, Van Baar J, Beardsley P, Willwacher T, Rao S, Forlines C. iLamps: geometrically aware and self-configuring projectors. In: ACM SIGGRAPH 2003 Papers. San Diego California: ACM; 2003. p. 809-18. Available from: https://dl.acm.org/doi/10.1145/1201775.882349.

[11] Park J, Lee BU. Defocus and geometric distortion correction for projected images on a curved surface. Applied Optics. 2016 Feb;55(4):896. Available from: https://opg.optica.org/abstract.cfm?URI=ao-55-4-896.

[12] Zhang Z. A flexible new technique for camera calibration. IEEE Transactions on Pattern Analysis and Machine Intelligence. 2000 Nov;22(11):1330-4. Available from: http://ieeexplore.ieee.org/document/888718/.

[13] Johnson T, Gyarfas F, Skarbez R, Towles H, Fuchs H. A Personal Surround Environment: Projective Display with Correction for Display Surface Geometry and Extreme Lens Distortion. In: 2007 IEEE Virtual Reality Conference. Charlotte, NC, USA: IEEE; 2007. p. 147-54. Available from: https://ieeexplore.ieee.org/document/4161017/.

[14] Ruigang Yang, Gotz D, Hensley J, Towles H, Brown MS. PixelFlex: a reconfigurable multi-projector display system. In: Proceedings Visualization, 2001. VIS '01. San Diego, CA, USA: IEEE; 2001. p. 167-554. Available from: http://ieeexplore.ieee.org/document/964508/.

[15] Ruigang Yang, Zhengyou Zhang. Model-based head pose tracking with stereovision. Proceedings of Fifth IEEE International Conference on Automatic Face Gesture Recognition, Automatic Face and Gesture Recognition, 2002 Proceedings Fifth IEEE International Conference on, Automatic face gesture recognition. 2002 Jan:255-60. Place: Piscataway, NJ, USA, USA Publisher: IEEE. Available from: https://research.ebsco.com/linkprocessor/plink?id=aea492ba-4222-314c-ac52-5ce6c22f5056.

[16] Wang X, Yan K. Automatic color correction for multi-projector display systems. Multimedia Tools and Applications. 2018 Jun;77(11):13115-32. Available from: http://link.springer.com/10.1007/s11042-017-4934-0.

[17] Brown M, Majumder A, Yang R. Camera-based calibration techniques for seamless multiprojector displays. IEEE Transactions on Visualization and Computer Graphics. 2005 Mar;11(2):193-206. Available from: http://ieeexplore.ieee.org/document/1388230/.

[18] Jiang C, Lim B, Zhang S. Three-dimensional shape measurement using a structured light system with dual projectors. Applied Optics. 2018 May;57(14):3983. Available from: https://opg.optica.org/abstract.cfm?URI=ao-57-14-3983.

[19] Wang H, Wu C, Jia T, Yu X. Projector calibration algorithm in omnidirectional structured light. In: Lv Y, Su J, Gong W, Yang J, Bao W, Chen W, et al., editors. LIDAR Imaging Detection and Target Recognition 2017. Changchun, China: SPIE; 2017. p. 131. Available from: https://www.spiedigitallibrary.org/conference-proceedings-of-spie/10605/2293993/Projector-calibration-algorithm-in-omnidirectional-structured-light/10.1117/12.2293993.full.

[20] Raij A, Gill G, Majumder A, Towles H, Fuchs H. Pixelflex2: A comprehensive, automatic, casually-aligned multi-projector display. In: IEEE International Workshop on Projector-Camera Systems; 2003. p. 203-11.

[21] Starkweather GK. DSHARP—a wide-screen multi-projector display. Journal of Optics A: Pure and Applied Optics. 2003 Sep;5(5):S136-9. Available from: https://iopscience.iop.org/article/10.1088/1464-4258/5/5/354.

[22] Raskar R, Van Baar J. P-153: Low-Cost Multi-Projector Curved Screen Displays. SID Symposium Digest of Technical Papers. 2005;36(1):884. Available from: http://doi.wiley.com/10.1889/1.2036590.

[23] Van Baar J, Willwacher T, Rao S, Raskar R. Seamless multi-projector display on curved screens. In: Proceedings of the workshop on Virtual environments 2003. Zurich Switzerland: ACM; 2003. p. 281-6. Available from: https://dl.acm.org/doi/10.1145/769953.769986.

[24] Sajadi B, Majumder A. Auto-calibration of cylindrical multi-projector systems. In: 2010 IEEE Virtual Reality Conference (VR). Boston, MA, USA: IEEE; 2010. p. 155-62. Available from: http://ieeexplore.ieee.org/document/5444797/.

[25] Xizuo L, Yan L, Xiaogang X, Liang M. Multi-Projector Calibration Based on Virtual Viewing Space. International Journal of Virtual Reality. 2019 Oct;19(3). Available from: https://ijvr.eu/article/view/2918.

[26] Askarian Bajestani S, Pourreza H, Nalbandian S. Scalable and view-independent calibration of multi-projector display for arbitrary uneven surfaces. Machine Vision and Applications. 2019 Oct;30(7-8):1191-207. Available from: http://link.springer.com/10.1007/s00138-019-01044-6.

[27] Zhao S, Dai S. Automatic Registration of Multi-Projector on Parameterized Surface in Two-Dimensionality. In: Proceedings of the 2019 International Conference on Modeling, Simulation, Optimization and Numerical Techniques (SMONT 2019). Shenzhen, China: Atlantis Press; 2019. Available from: https://www.atlantis-press.com/article/55917621.

[28] Zhao S, Zhao M, Dai S. Automatic Registration of Multi-Projector Based on Coded Structured Light. Symmetry. 2019 Nov;11(11):1397. Available from: https://www.mdpi.com/2073-8994/11/11/1397.

[29] Wang X, Yan K, Liu Y. Automatic geometry calibration for multi-projector display systems with arbitrary continuous curved surfaces. IET Image Processing. 2019 May;13(7):1050-5. Available from: https://ietresearch.onlinelibrary.wiley.com/doi/10.1049/iet-ipr.2018.5575.

[30] Huang TH, Wang TC, Chen HH. Radiometric Compensation of Images Projected on Non-White Surfaces by Exploiting Chromatic Adaptation and Perceptual Anchoring. IEEE Transactions on Image Processing. 2017 Jan;26(1):147-59. Available from: http://ieeexplore.ieee.org/document/7515212/.

[31] Heinz M, Brunnett G. Dense sampling of 3D color transfer functions using HDR photography. In: 2015 IEEE Conference on Computer Vision and Pattern Recognition Workshops (CVPRW). Boston, MA, USA: IEEE; 2015. p. 25-32. Available from: http://ieeexplore.ieee.org/document/7301372/.

[32] Menk C, Koch R. Truthful Color Reproduction in Spatial Augmented Reality Applications. IEEE Transactions on Visualization and Computer Graphics. 2012:1-1. Available from: https://ieeexplore.ieee.org/document/6298886.

[33] Jones BR, Sodhi R, Budhiraja P, Karsch K, Bailey B, Forsyth D. Projectibles: Optimizing Surface Color For Projection. In: Proceedings of the 28th Annual ACM Symposium on User Interface Software & Technology. Charlotte NC USA: ACM; 2015. p. 137-46. Available from: https://dl.acm.org/doi/10.1145/2807442.2807486.

[34] Pjanic P, Grundhofer A. Paxel: A Generic Framework to Superimpose High-Frequency Print Patterns Using Projected Light. IEEE Transactions on Image Processing. 2018 Jul;27(7):3541-55. Available from: https://ieeexplore.ieee.org/document/8332945/.

[35] Majumder A, Stevens R. LAM: luminance attenuation map for photometric uniformity in projection based displays. In: Proceedings of the ACM symposium on Virtual reality software and technology. Hong Kong China: ACM; 2002. p. 147-54. Available from: https://dl.acm.org/doi/10.1145/585740.585765.

[36] Ramasubramanian M, Pattanaik SN, Greenberg DP. A perceptually based physical error metric for realistic image synthesis. In: Proceedings of the 26th annual conference on Computer graphics and interactive techniques - SIGGRAPH '99. Not Known: ACM Press; 1999. p. 73-82. Available from: http://portal.acm.org/citation.cfm?doid=311535.311543.

[37] Dong Wang, Sato I, Okabe T, Sato Y. Radiometric Compensation in a Projector-Camera System Based Properties of Human Vision System. In: 2005 IEEE Computer Society Conference on Computer Vision and Pattern Recognition (CVPR'05) - Workshops. vol. 3. San Diego, CA, USA: IEEE; 2005. p. 100-0. Available from: http://ieeexplore.ieee.org/document/1565410/.

[38] Majumder A, Stevens R. Perceptual photometric seamlessness in projection-based tiled displays. ACM Transactions on Graphics. 2005 Jan;24(1):118-39. Available from: https://dl.acm.org/doi/10.1145/1037957.1037964.

[39] Debevec PE, Malik J. Recovering high dynamic range radiance maps from photographs. In: ACM SIGGRAPH 2008 classes. Los Angeles California: ACM; 2008. p. 1-10. Available from: https://dl.acm.org/doi/10.1145/1401132.1401174.